

Pressure induced enhancement of polar distortions in a metal, and implications on the Rashba spin-splitting

Evie Ladbrook,¹ Urmimala Dey,^{2,3} Nicholas C. Bristowe,² Robin S. Perry,⁴ Dominik Daisenberger,⁵ Mark R. Warren,⁵ and Mark S. Senn^{1,*}

¹*Department of Chemistry, University of Warwick, Gibbet Hill, Coventry, CV4 7AL, United Kingdom*

²*Centre for Materials Physics, Durham University, South Road, Durham DH1 3LE, United Kingdom*

³*Luxembourg Institute of Science and Technology (LIST),*

Avenue des Hauts-Fourneaux 5, L-4362, Esch-sur-Alzette, Luxembourg

⁴*London Centre for Nanotechnology and Department of Physics and Astronomy, University College London, London WC1E 6BT, United Kingdom*

⁵*Diamond Light Source Ltd, Harwell Science and Innovation Campus, Didcot OX11 0DE, United Kingdom*

(Dated: February 3, 2025)

Polar metals are an intriguing class of materials in which electric polarisation and metallicity can coexist within a single phase. The unique properties of polar metals challenge expectations, making way for the exploration of exotic phenomena such as unconventional magnetism, hyperferroelectric multiferroicity and developing multifunctional devices that can leverage both the materials electric polarization and its asymmetry in the spin conductivity, that arises due to the Rashba effect. Here, via a high pressure single crystal diffraction study, we report the pressure-induced enhancement of polar distortions in such a metal, $\text{Ca}_3\text{Ru}_2\text{O}_7$. Our DFT calculations highlight that naive assumptions about the linear dependency between polar distortion amplitudes and the magnitude of the Rashba spin splitting may not be generally valid.

Polar metals are an intriguing class of materials in which electric polarisation and metallicity can coexist within a single phase. The concept of a ferroelectric-like transition in a metal was first predicted in 1965 [1] but not experimentally realised until such a transition was identified in metallic LiOsO_3 [2]. Several polar metals have been identified since then [3–5], with ferroelectric switching first being demonstrated in WTe_2 [6, 7], defying assumptions that ferroelectricity and metallicity are mutually exclusive. The unique properties of polar metals do not only challenge expectations, making way for the exploration of exotic phenomena such as unconventional magnetism [8], hyperferroelectric multiferroicity [9] and unique topologies [10], but also open up the possibility for developing multifunctional devices [4, 11–13] that can leverage both electric polarisation, or ferroelectricity, and metallic conductivity.

The absence of an inversion centre in combination with the spin orbit interaction can facilitate the Rashba interaction. As polar metals can satisfy both requirements, they provide an obvious platform to explore this effect. Although the Rashba interaction has most commonly been studied at surfaces and interfaces [14, 15], where inversion symmetry is necessarily broken, the effect has also been demonstrated in bulk systems [16–18]. This has implications to the field of spintronics [19], where electron spins, rather than just the charge, may be manipulated by an electric field.

In many polar metals, the polar mode arises through a ‘geometric mechanism’ as conventional chemical mechanisms for ferroelectricity are broadly incompatible with

metallicity [3, 4, 20, 21]. Typically, free electrons would screen the long-range interactions responsible for ferroelectricity, inhibiting formation of a permanent electric dipole. However, materials in which a polar mode arises due to a structural instability may circumvent this. One mechanism is via a ‘hybrid improper’ mechanism [22], prototypical to $n = 2$ Ruddlesden-Popper (RP) phase $\text{Ca}_3\text{Mn}_2\text{O}_7$, where polarisation arises due to the trilinear coupling between two non-polar structural distortions, tilting and rotation of the MnO_6 octahedra in the case of $\text{Ca}_3\text{Mn}_2\text{O}_7$, with a polar distortion mode, as shown in Fig 1.

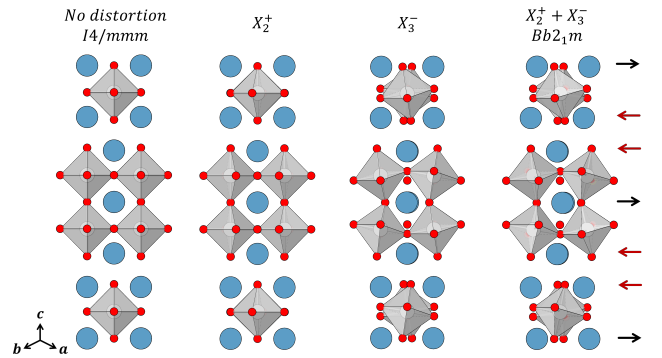


FIG. 1. $n = 2$ Ruddlesden-Popper structure consisting of two perovskite layers separated by a rock-salt-like layer with representation of the distortion of the theoretical high symmetry $I4/mmm$ to the orthorhombic $Bb2_1m$ phase through octahedral rotations (X_2^+) and tilts (X_3^-). Arrows indicate the polar distortions, primarily consisting of Ca displacements.

* m.senn@warwick.ac.uk

$\text{Ca}_3\text{Ru}_2\text{O}_7$ is a member of the $n = 2$ RP family, crystallizing in the polar $Bb2_1m$ space group (non-standard

setting of $Cmc2_1$), however, it has a metallic ground state [23, 24]. Although ferroelectric switching cannot be achieved by application of an external electric field, a recent study has revealed a polar domain structure consisting of 90- and 180-degree domain walls with ferroelastic domains that can be switched by applied uniaxial strain [24]. $\text{Ca}_3\text{Ru}_2\text{O}_7$ also undergoes a spin reorientation transition where, upon cooling from 60 to 48 K, the spins reorient from aligning along the crystallographic a axis, aligning ferromagnetically within each perovskite layer and antiferromagnetically between them, to be parallel to b [23, 25, 26]. The coupling between the spin ordering direction and the polar crystallographic axis via a strong spin-orbit interaction induces the Rashba-like spin splitting in momentum space [27]. Very recently, it has been shown that this transition can be induced by application of uniaxial strain which emphasizes how the structural, magnetic and electronic degrees of freedom are intricately coupled [28].

Similarly, pressure can be used to directly probe the interplay between the structural, octahedral rotations and tilts [29], and polar distortions with a view to understanding how the Rashba spin splitting might be tuned in polar metals. Although it is generally understood that the initial application of hydrostatic pressure suppresses polarisation in conventional proper ferroelectrics, such as BaTiO_3 [30, 31], as they tend to undergo a phase transition to a non-polar state, this does not necessarily hold true for all ferroelectrics. For example, in the case of the hybrid improper mechanism, we have recently shown, by powder X-ray diffraction in combination with density functional theory calculations (DFT), that polarisation can be enhanced in the insulator $\text{Ca}_3\text{Ti}_2\text{O}_7$ by pressure [32].

The prospect of coupling spin transport properties to external stimuli like pressure via internal structural degrees of freedom, such as octahedral rotations, and their coupling to polar modes, is intriguing. However, naively, we might assume that the amplitude of the Rashba effect has a linear dependence on the polar mode, as shown for surfaces, interfaces and bulk systems [33–37], however, there are indications in the literature that this situation may be somewhat more complex [38].

Here we report the result of our high-pressure single crystal diffraction studies on $\text{Ca}_3\text{Ru}_2\text{O}_7$ that show that the structural ingredients, necessary for enhancing the amplitude of the polar mode in a metal, are systematically enhanced up to 15 GPa. Our first-principles calculations within density functional theory (DFT) reveal that, contrary to expectations, the enhancement of the polar mode manifests itself in a decrease in spin splitting in momentum space.

Single crystal samples were selected from the same growth batch as those which demonstrated incommensurate magnetism at 50K [39]. All samples were confirmed as single phase and good quality via magnetisation, resistivity and SEM/EDX measurements.

A single crystal of dimensions $50 \times 30 \times 15 \mu\text{m}$ was loaded into a LeToullec diamond anvil cell (DAC)

equipped with Boehler-Almax anvils with $400 \mu\text{m}$ culets and a rhenium gasket which was pre-indented to $50 \mu\text{m}$ with a $250 \mu\text{m}$ diameter sample chamber eroded into the indent. Helium was used as a pressure transmitting medium to ensure the sample was compressed under hydrostatic pressure. A ruby sphere was used as pressure indicator [40]. Single crystal X-ray diffraction measurements were performed using a four-axis Newport diffractometer equipped with a Dectris Eiger CdTe detector, operating at a wavelength of $\lambda = 0.4859 \text{ \AA}$ (corresponding to a beam energy of approximately 25.5 keV), in Experimental Hutch 2 (EH2) at Beamline I19 of the Diamond Light Source.

Indexing, integration and refinement were performed using CrysAlisPRO with a spherical absorption correction. The structure was initially solved for the ambient pressure collection using SHELXT [41] and subsequent pressures by isomorphous replacement, and then refined to convergence using SHELXL [42] implemented through Olex2 [43]. The presence of inversion twinning was accounted for via the $([-1\ 0\ 0], [0\ -1\ 0], [0\ 0\ 1])$ twin law for which the batch scale factor (BASF) was fixed to 0.50.

High pressure single crystal X-ray diffraction data were collected between 0 and 14.5(2) GPa. Fig 2 shows how the experimentally refined a and b lattice parameters and volume evolve with pressure compared to those calculated from DFT. Full computational details can be found in the Supplemental Material (SM) [44]. In both cases, the lattice parameters and volume decrease smoothly with pressure. Experimentally, we find a slightly greater compressibility in b , and smaller in a , compared to that calculated by DFT. However, this could be because the DFT calculations were performed at 0 K whilst experimental measurements were carried out at room temperature. Compressibility parameters and Birch-Murnaghan coefficients were calculated using PASCAL [45] and are tabulated in the Supplemental Material [Tables S2 and S3 [44]].

To explore the evolution of the atomic level structure, the experimental and DFT-relaxed structures were then decomposed in terms of symmetry-adapted displacements using ISODISTORT [46, 47]. The $Bb2_1m$ phase is related to the theoretical $I4/mmm$ aristotype by an in-phase rotation and an out-of-phase tilt of the TiO_6 octahedra which transform as irreducible representations X_2^+ and X_3^- , respectively. These couple to the polar displacement, which transforms as irreducible representation Γ_5^- , via the trilinear coupling mechanism. The resulting pressure dependent symmetry distortion mode amplitudes are shown in Fig 3.

The experimentally determined mode amplitudes show an overall steady increase in the amplitude of the rotation, X_2^+ , whilst the amplitude of the tilt, X_3^- , remains relatively constant as the pressure increases. Despite some fluctuations in the experimentally determined mode amplitudes due to restrictions concerning the experimental set up, such as narrow opening angle of the DACs, these results show a good level of agreement with the DFT calculated mode amplitudes. In accordance with

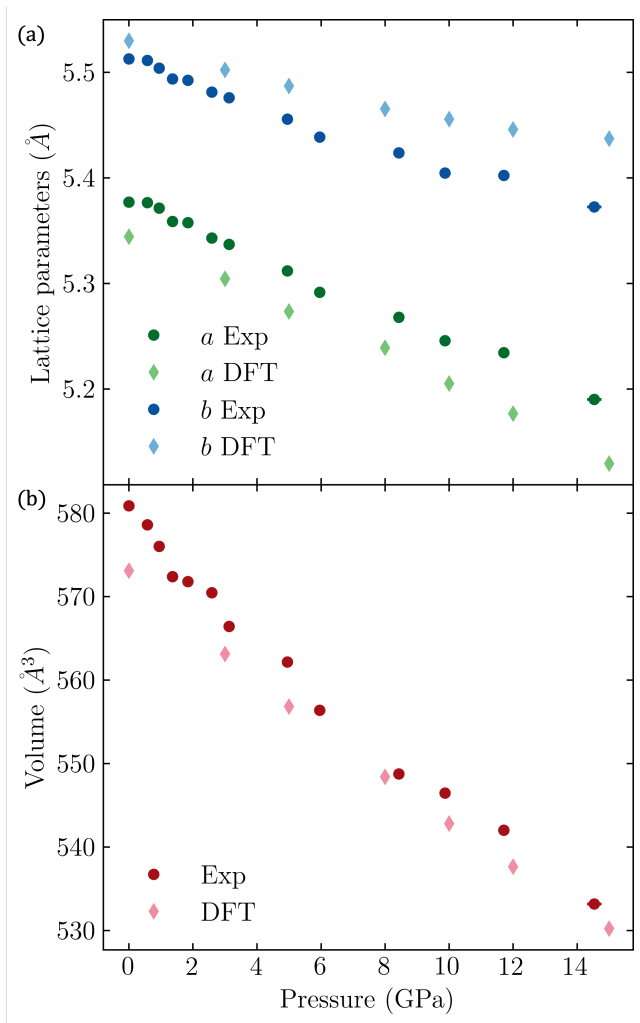


FIG. 2. (a) a and b lattice parameters and (b) unit cell volume extracted from variable pressure single crystal diffraction data and DFT calculations.

the trilinear coupling mechanism, the amplitude of the polar distortion, Γ_5^- , should be linearly proportional to the product of the driving order parameters, X_2^+ and X_3^- , which is demonstrated in the inset of Fig 3, showing a linear trend with an intercept at zero [22]. This confirms that, for the experimental data, the polarisation is driven solely by the hybrid improper mechanism. However, for the DFT calculated results, the Γ_5^- amplitude is in excess of that expected by the trilinear mechanism. This suggests that there is a small proper contribution to the polarisation, which, as shown in Fig. S3 [44], vanishes as the pressure increases above 10 GPa. This could be for a variety of reasons such as the difference in volume of the DFT unit cell, dependence on the pseudopotentials or exchange correlation functional or it could be a real discrepancy between 0 K DFT and our room temperature diffraction experiments. However, in general, the level of agreement, especially considering both the complexity of the electronic structure of these materials and the challenges of perform-

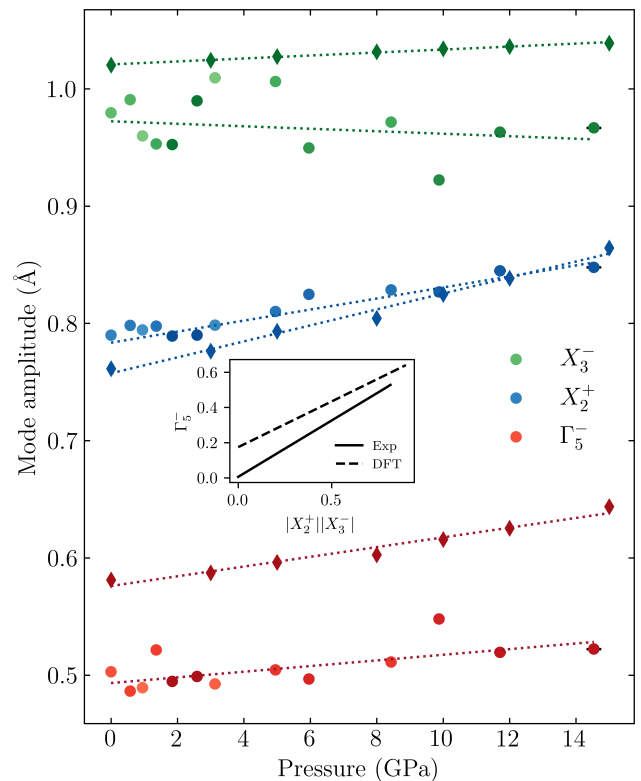


FIG. 3. Distortion mode amplitudes as a function of pressure for experimental (circles) and DFT calculated (diamonds) results. For the experimental results, a weighted linear regression was performed based on the R_1 statistic of the refined structures, with darker colours indicating a lower R_1 value. The inset shows a plot of the product of the amplitude of the rotation (X_2^+) and tilt (X_3^-) modes, from these fits, against the polar mode (Γ_5^-) amplitude.

ing high resolution x-ray diffraction at these pressures, is very good. The key point from both the experimental and DFT work is that that octahedral rotations are enhanced at a greater rate than the octahedral tilts are suppressed, resulting in an increase in the polarisation via the trilinear mechanism. While this pressure induced enhancement would be unexpected for a proper ferroelectric, we have recently predicted, via DFT calculations, a similar effect in insulating hybrid improper ferroelectric $\text{Ca}_3\text{Ti}_2\text{O}_7$ [32], and thus our experimental and DFT results are suggestive that this phenomena may be much more wide spread.

Motivated by our ability to enhance the polar distortion in this material as a function of pressure, we now turn our attention to the effect such enhancements might have on the band structure of these materials.

Figs. 4(a-b) present the band structures calculated for the ambient-pressure $Bb2_1m$ structure of $\text{Ca}_3\text{Ru}_2\text{O}_7$ along the $-M_x - \Gamma - M_x$ direction with and without spin-orbit coupling (SOC). We observe a sizeable Rashba splitting of the bands around the Γ -point near the valence band maximum (VBM) when SOC is turned on.

To quantify the magnitude of the momentum-

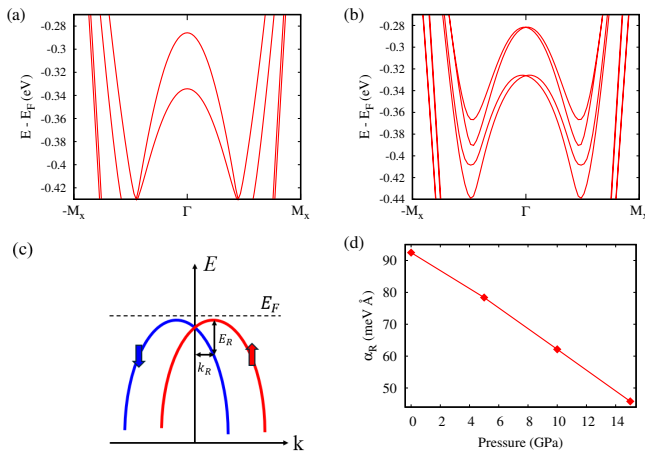


FIG. 4. Electronic band structure calculated at ambient pressure (a) without and (b) with SOC. E_F is the Fermi energy. (c) Schematic diagram illustrating the definition of Rashba parameter, where k_R is the distance between the crossing point of the Rashba spin-split bands and VBM, and E_R is the corresponding energy difference. Red and blue arrows indicate the up and down spin-character of the bands, respectively. (d) Evolution of the Rashba parameter α_R in $\text{Ca}_3\text{Ru}_2\text{O}_7$ as a function of pressure.

dependent Rashba splitting, we compute the Rashba parameter defined as $\alpha_R = 2E_R/k_R$, where k_R is the distance between the crossing point of the Rashba-split bands and VBM, and E_R is the corresponding energy splitting [33, 34], as shown in Fig. 4(c). Surprisingly, the Rashba parameter calculated for the fully relaxed structures at different pressures reveal a monotonic decrease in α_R with increasing pressure [Fig. 4(d)]. Since the polar mode amplitude in $\text{Ca}_3\text{Ru}_2\text{O}_7$ increases with pressure [Fig 3], this observation contradicts the conventional expectation that the Rashba parameter should scale with the polar mode amplitude [33–37]. In fact, the increase in the amplitude of the polar mode appears to be the primary cause of the reduction in the Rashba parameter. As detailed in S7 [44], when the polar mode is absent, leaving only rotation and tilt modes, which by themselves break inversion symmetry, the Rashba parameter is enhanced compared to its value when the po-

lar mode is present. Unpicking the multiple complexities of the pressure-dependent structure, and band structure, represent substantial further work, but our result is strongly suggestive that the magnitude of the structural polarisation is an insufficient proxy for the k-space spin-polarisation dependence.

In conclusion, we have performed a detailed high pressure investigation into the pressure dependence of the hybrid improper ordering parameters in polar metal, $\text{Ca}_3\text{Ru}_2\text{O}_7$. Our results show that, contrary to the situation predominantly observed for proper ferroelectrics, hydrostatic pressure actually acts to enhance the polar distortions in this materials. This comes about due to the increase in the magnitude of RuO_6 octahedral rotations, which form one of the primary order parameters of the hybrid improper mechanism. Curiously, despite the enhanced magnitude of the polar mode at high pressures, our theoretical calculations show that, counterintuitively, this would lead to a decrease in the Rashba spin-splitting. Thus, our results highlight the Rashba effect in polar metals as a distinctive phenomenon worthy of further investigation.

ACKNOWLEDGMENTS

E.L. thanks the University of Warwick for a PhD studentship through the Warwick Centre for Doctoral Training in Analytical Science and thanks Matt Edwards for assistance in the collection of high pressure X-ray diffraction data. U.D. and N.C.B. acknowledge the Leverhulme Trust for a research project grant (Grant No. RPG-2020-206). This work used the ARCHER2 UK National Supercomputing Service (<https://www.archer2.ac.uk>) [48] and the Hamilton HPC Service of Durham University. M.S.S. acknowledges the Royal Society for a fellowship (UF160265 & URF\R\231012) and EPSRC grant “Novel Multiferroic Perovskites through Systematic Design” (EP/S027106/1) for funding. The initial high pressure diffraction studies were performed via the the Warwick X-ray Research Technology Platform. We acknowledge Diamond Light Source for time on beamline I19 under proposal CY36775.

[1] P. W. Anderson and E. I. Blount, Symmetry Considerations on Martensitic Transformations: “Ferroelectric” Metals?, *Physical Review Letters* **14**, 217 (1965).
 [2] Y. Shi, Y. Guo, X. Wang, A. J. Princep, D. Khalyavin, P. Manuel, Y. Michiue, A. Sato, K. Tsuda, S. Yu, M. Arai, Y. Shirako, M. Akaogi, N. Wang, K. Yamaura, and A. T. Boothroyd, A ferroelectric-like structural transition in a metal, *Nature Materials* **12**, 1024 (2013).
 [3] T. H. Kim, D. Puggioni, Y. Yuan, L. Xie, H. Zhou, N. Campbell, P. J. Ryan, Y. Choi, J.-W. Kim, J. R. Patzner, S. Ryu, J. P. Podkaminer, J. Irwin, Y. Ma, C. J. Fennie, M. S. Rzchowski, X. Q. Pan, V. Gopalan, J. M.

Rondinelli, and C. B. Eom, Polar metals by geometric design, *Nature* **533**, 68 (2016).
 [4] D. Puggioni and J. M. Rondinelli, Designing a robustly metallic noncentrosymmetric ruthenate oxide with large thermopower anisotropy, *Nature Communications* **5**, 3432 (2014).
 [5] T. Kolodiazny, Insulator-metal transition and anomalous sign reversal of the dominant charge carriers in perovskite $\text{BaTiO}_{3-\delta}$, *Physical Review B* **78**, 045107 (2008).
 [6] Z. Fei, W. Zhao, T. A. Palomaki, B. Sun, M. K. Miller, Z. Zhao, J. Yan, X. Xu, and D. H. Cobden, Ferroelectric switching of a two-dimensional metal, *Nature* **560**, 336

- (2018).
- [7] P. Sharma, F.-X. Xiang, D.-F. Shao, D. Zhang, E. Y. Tsymbal, A. R. Hamilton, and J. Seidel, A room-temperature ferroelectric semimetal, *Science Advances* **5**, eaax5080 (2019).
 - [8] S. Lei, S. Chikara, D. Puggioni, J. Peng, M. Zhu, M. Gu, W. Zhao, Y. Wang, Y. Yuan, H. Akamatsu, M. H. W. Chan, X. Ke, Z. Mao, J. M. Rondinelli, M. Jaime, J. Singleton, F. Weickert, V. S. Zapf, and V. Gopalan, Comprehensive magnetic phase diagrams of the polar metal $\text{Ca}_3(\text{Ru}_{0.95}\text{Fe}_{0.05})_2\text{O}_7$, *Physical Review B* **99**, 224411 (2019).
 - [9] W. Luo, K. Xu, and H. Xiang, Two-dimensional hyperferroelectric metals: A different route to ferromagnetic-ferroelectric multiferroics, *Physical Review B* **96**, 235415 (2017).
 - [10] S.-Y. Xu, I. Belopolski, N. Alidoust, M. Neupane, G. Bian, C. Zhang, R. Sankar, G. Chang, Z. Yuan, C.-C. Lee, S.-M. Huang, H. Zheng, J. Ma, D. S. Sanchez, B. Wang, A. Bansil, F. Chou, P. P. Shibayev, H. Lin, S. Jia, and M. Z. Hasan, Discovery of a Weyl fermion semimetal and topological Fermi arcs, *Science* **349**, 613 (2015).
 - [11] D. Puggioni, G. Giovannetti, M. Capone, and J. M. Rondinelli, Design of a Mott Multiferroic from a Nonmagnetic Polar Metal, *Physical Review Letters* **115**, 087202 (2015).
 - [12] Q.-F. Yao, J. Cai, W.-Y. Tong, S.-J. Gong, J.-Q. Wang, X. Wan, C.-G. Duan, and J. H. Chu, Manipulation of the large Rashba spin splitting in polar two-dimensional transition-metal dichalcogenides, *Physical Review B* **95**, 165401 (2017).
 - [13] X. Liu, Y. Yang, T. Hu, G. Zhao, C. Chen, and W. Ren, Vertical ferroelectric switching by in-plane sliding of two-dimensional bilayer WTe_2 , *Nanoscale* **11**, 18575 (2019).
 - [14] K. Shanavas and S. Satpathy, Electric Field Tuning of the Rashba Effect in the Polar Perovskite Structures, *Physical Review Letters* **112**, 086802 (2014).
 - [15] S. Bhowal and S. Satpathy, Electric field tuning of the anomalous Hall effect at oxide interfaces, *npj Computational Materials* **5**, 1 (2019).
 - [16] D. Di Sante, P. Barone, R. Bertacco, and S. Picozzi, Electric Control of the Giant Rashba Effect in Bulk GeTe , *Advanced Materials* **25**, 509 (2013).
 - [17] K. Ishizaka, M. S. Bahramy, H. Murakawa, M. Sakano, T. Shimojima, T. Sonobe, K. Koizumi, S. Shin, H. Miyahara, A. Kimura, K. Miyamoto, T. Okuda, H. Namatame, M. Taniguchi, R. Arita, N. Nagaosa, K. Kobayashi, Y. Murakami, R. Kumai, Y. Kaneko, Y. Onose, and Y. Tokura, Giant Rashba-type spin splitting in bulk BiTeI , *Nature Materials* **10**, 521 (2011).
 - [18] K. Yamauchi, P. Barone, and S. Picozzi, Bulk Rashba effect in multiferroics: A theoretical prediction for BiCoO_3 , *Physical Review B* **100**, 245115 (2019).
 - [19] A. Manchon, H. C. Koo, J. Nitta, S. M. Frolov, and R. A. Duine, New perspectives for Rashba spin-orbit coupling, *Nature Materials* **14**, 871 (2015).
 - [20] S. Bhowal and N. A. Spaldin, Polar Metals: Principles and Prospects, *Annual Review of Materials Research* **53**, 53 (2023).
 - [21] N. A. Benedek and T. Birol, ‘Ferroelectric’ metals reexamined: fundamental mechanisms and design considerations for new materials, *Journal of Materials Chemistry C* **4**, 4000 (2016).
 - [22] N. A. Benedek and C. J. Fennie, Hybrid Improper Ferroelectricity: A Mechanism for Controllable Polarization-Magnetization Coupling, *Physical Review Letters* **106**, 107204 (2011).
 - [23] G. Cao, S. McCall, J. E. Crow, and R. P. Guertin, Observation of a Metallic Antiferromagnetic Phase and Metal to Nonmetal Transition in $\text{Ca}_3\text{Ru}_2\text{O}_7$, *Physical Review Letters* **78**, 1751 (1997).
 - [24] S. Lei, M. Gu, D. Puggioni, G. Stone, J. Peng, J. Ge, Y. Wang, B. Wang, Y. Yuan, K. Wang, Z. Mao, J. M. Rondinelli, and V. Gopalan, Observation of Quasi-Two-Dimensional Polar Domains and Ferroelastic Switching in a Metal, $\text{Ca}_3\text{Ru}_2\text{O}_7$, *Nano Letters* **18**, 3088 (2018).
 - [25] W. Bao, Z. Q. Mao, Z. Qu, and J. W. Lynn, Spin Valve Effect and Magnetoresistivity in Single Crystalline $\text{Ca}_3\text{Ru}_2\text{O}_7$, *Physical Review Letters* **100**, 247203 (2008).
 - [26] B. Bohnenbuck, I. Zegkinoglou, J. Stremper, C. Schüßler-Langeheine, C. S. Nelson, P. Leininger, H.-H. Wu, E. Schierle, J. C. Lang, G. Srajer, S. I. Ikeda, Y. Yoshida, K. Iwata, S. Katano, N. Kikugawa, and B. Keimer, Magnetic structure and orbital state of $\text{Ca}_3\text{Ru}_2\text{O}_7$ investigated by resonant x-ray diffraction, *Physical Review B* **77**, 224412 (2008).
 - [27] I. Marković, M. D. Watson, O. J. Clark, F. Mazzola, E. Abarca Morales, C. A. Hooley, H. Rosner, C. M. Polley, T. Balasubramanian, S. Mukherjee, N. Kikugawa, D. A. Sokolov, A. P. Mackenzie, and P. D. C. King, Electronically driven spin-reorientation transition of the correlated polar metal $\text{Ca}_3\text{Ru}_2\text{O}_7$, *Proceedings of the National Academy of Sciences* **117**, 15524 (2020).
 - [28] C. D. Dashwood, A. H. Walker, M. P. Kwasigroch, L. S. I. Veiga, Q. Faure, J. G. Vale, D. G. Porter, P. Manuel, D. D. Khalyavin, F. Orlandi, C. V. Colin, O. Fabelo, F. Krüger, R. S. Perry, R. D. Johnson, A. G. Green, and D. F. McMorrow, Strain control of a bandwidth-driven spin reorientation in $\text{Ca}_3\text{Ru}_2\text{O}_7$, *Nature Communications* **14**, 6197 (2023).
 - [29] S. P. Ramkumar and E. A. Nowadnick, Octahedral rotations in Ruddlesden-Popper layered oxides under pressure from first principles, *Physical Review B* **104**, 144105 (2021).
 - [30] T. Ishidate, S. Abe, H. Takahashi, and N. Mōri, Phase Diagram of BaTiO_3 , *Physical Review Letters* **78**, 2397 (1997).
 - [31] E. Bousquet and P. Ghosez, First-principles study of barium titanate under hydrostatic pressure, *Physical Review B* **74**, 180101 (2006).
 - [32] G. Clarke, D. Daisenberger, X. Luo, S. W. Cheong, N. C. Bristowe, and M. S. Senn, Pressure-dependent phase transitions in hybrid improper ferroelectric Ruddlesden-Popper oxides, *Physical Review B* **109**, 094107 (2024).
 - [33] L. Leppert, S. E. Reyes-Lillo, and J. B. Neaton, Electric Field- and Strain-Induced Rashba Effect in Hybrid Halide Perovskites, *The Journal of Physical Chemistry Letters* **7**, 3683 (2016).
 - [34] L. G. D. da Silveira, P. Barone, and S. Picozzi, Rashba-Dresselhaus spin-splitting in the bulk ferroelectric oxide BiAlO_3 , *Physical Review B* **93**, 245159 (2016).
 - [35] P. Z. Hanakata, A. S. Rodin, H. S. Park, D. K. Campbell, and A. H. Castro Neto, Strain-induced gauge and Rashba fields in ferroelectric Rashba lead chalcogenide PbX monolayers ($\text{X}=\text{S}, \text{Se}, \text{Te}$), *Physical Review B* **97**, 235312 (2018).
 - [36] P. Noël, F. Trier, L. M. Vicente Arche, J. Bréhin, D. C. Vaz, V. Garcia, S. Fusil, A. Barthélémy, L. Vila, M. Bibes, and J.-P. Attané, Non-volatile electric control

- of spin-charge conversion in a SrTiO₃ Rashba system, *Nature* **580**, 483 (2020).
- [37] Y. Jin, J. Li, G. Wang, Q. Zhang, Z. Liu, and X. Mao, Giant tunable Rashba spin splitting in two-dimensional polar perovskites TlSnX₃ (X = Cl, Br, I), *Physical Chemistry Chemical Physics* **24**, 17561 (2022).
- [38] X. Wang, X. Li, H. Tian, H. Sang, J.-M. Liu, and Y. Yang, Anomalous Rashba Effect Driven by Polar and Nonpolar Modes in the Ferroelectric Superlattice, *The Journal of Physical Chemistry C* **126**, 20620 (2022).
- [39] Q. Faure, C. D. Dashwood, C. V. Colin, R. D. Johnson, E. Ressouche, G. B. G. Stenning, J. Spratt, D. F. McMorrow, and R. S. Perry, Magnetic structure and field dependence of the cycloid phase mediating the spin reorientation transition in Ca₃Ru₂O₇, *Physical Review Research* **5**, 013040 (2023).
- [40] K. Syassen, Ruby under pressure, *High Pressure Research* **28**, 75 (2008).
- [41] G. M. Sheldrick, *SHELXT* – Integrated space-group and crystal-structure determination, *Acta Crystallographica Section A: Foundations and Advances* **71**, 3 (2015).
- [42] G. M. Sheldrick, Crystal structure refinement with SHELXL, *Acta Crystallographica Section C: Structural Chemistry* **71**, 3 (2015).
- [43] O. V. Dolomanov, L. J. Bourhis, R. J. Gildea, J. a. K. Howard, and H. Puschmann, OLEX2: a complete structure solution, refinement and analysis program, *Journal of Applied Crystallography* **42**, 339 (2009).
- [44] See Supplemental Material at [URL will be inserted by publisher] for high pressure CIFs, refinement statistics, compressibility parameters, Birch-Murnaghan coefficients and full computational details including the determination of the magnetic ground state and ambient band structure and the evolution of the band structure, magnetic moment and Rashba spin splitting with pressure. The Supplemental Material also contains Refs. [23, 25–27, 47, 49–59].
- [45] M. J. Cliffe and A. L. Goodwin, PASCAL: a principal axis strain calculator for thermal expansion and compressibility determination, *Journal of Applied Crystallography* **45**, 1321 (2012).
- [46] Campbell, B. J., Stokes, H. T., Tanner, D. E., and Hatch, D. M., ISODISPLACE: A web-based tool for exploring structural distortions., *Journal of Applied Crystallography* **39**, 607 (2006).
- [47] H. T. Stokes, D. M. Hatch, and B. J. Campbell, ISOTROPY Software Suite, iso.byu.edu.
- [48] G. Beckett, J. Beech-Brandt, K. Leach, Z. Payne, A. Simpson, L. Smith, A. Turner, and A. Whiting, ARCHER2 Service Description. Zenodo. (2024).
- [49] S. Patel, U. Dey, N. P. Adhikari, and A. Taraphder, Electric field and strain-induced band-gap engineering and manipulation of the Rashba spin splitting in Janus van der Waals heterostructures, *Phys. Rev. B* **106**, 035125 (2022).
- [50] G. Kresse and J. Furthmüller, Efficiency of ab-initio total energy calculations for metals and semiconductors using a plane-wave basis set, *Comput. Mater. Sci.* **6**, 15 (1996).
- [51] G. Kresse and J. Furthmüller, Efficient iterative schemes for ab initio total-energy calculations using a plane-wave basis set, *Phys. Rev. B* **54**, 11169 (1996).
- [52] J. P. Perdew, A. Ruzsinszky, G. I. Csonka, O. A. Vydrov, G. E. Scuseria, L. A. Constantin, X. Zhou, and K. Burke, Restoring the Density-Gradient Expansion for Exchange in Solids and Surfaces, *Phys. Rev. Lett.* **100**, 136406 (2008).
- [53] P. E. Blöchl, Projector augmented-wave method, *Phys. Rev. B* **50**, 17953 (1994).
- [54] G. Kresse and D. Joubert, From ultrasoft pseudopotentials to the projector augmented-wave method, *Phys. Rev. B* **59**, 1758 (1999).
- [55] S. L. Dudarev, G. A. Botton, S. Y. Savrasov, C. J. Humphreys, and A. P. Sutton, Electron-energy-loss spectra and the structural stability of nickel oxide: An LSDA+U study, *Phys. Rev. B* **57**, 1505 (1998).
- [56] K. Momma and F. Izumi, VESTA 3 for three-dimensional visualization of crystal, volumetric and morphology data, *J. Appl. Cryst.* **44**, 1272 (2011).
- [57] D. Puggioni, M. Horio, J. Chang, and J. M. Rondinelli, Cooperative interactions govern the fermiology of the polar metal Ca₃Ru₂O₇, *Phys. Rev. Res.* **2**, 023141 (2020).
- [58] M. Horio, Q. Wang, V. Granata, K. Kramer, Y. Sassa, S. Jöhr, D. Sutter, A. Bold, L. Das, Y. Xu, *et al.*, Electronic reconstruction forming a C 2-symmetric Dirac semimetal in Ca₃Ru₂O₇, *npj Quantum Materials* **6**, 29 (2021).
- [59] A. M. León, J. W. González, and H. Rosner, Ca₃Ru₂O₇: Interplay among degrees of freedom and the role of the exchange correlation, *Phys. Rev. Mater.* **8**, 024411 (2024).

SUPPLEMENTAL MATERIAL

TABLE S1. Lattice parameters and refinement statistics

Pressure (GPa)	a (Å)	b (Å)	c (Å)	R_1	wR_2	R_{int}	Goof
0.00(5)	5.3770(5)	5.5126(13)	19.60(4)	5.51	11.76	2.70	1.23
0.58(5)	5.3764(5)	5.5112(12)	19.53(6)	5.00	12.89	2.88	1.203
0.95(9)	5.3713(5)	5.5038(15)	19.48(6)	6.58	15.28	2.48	1.222
1.36(9)	5.3587(10)	5.494(2)	19.44(10)	4.61	12.90	3.02	1.248
1.84(13)	5.3576(5)	5.4924(10)	19.43(7)	1.98	5.54	1.91	1.272
2.59(13)	5.3429(7)	5.4812(17)	19.48(8)	1.98	6.32	1.85	1.230
3.13(17)	5.3370(7)	5.476(2)	19.38(8)	6.13	13.12	4.17	1.344
4.95(13)	5.3119(6)	5.4556(14)	19.40(6)	4.54	10.14	3.18	1.151
5.96(13)	5.2915(8)	5.439(2)	19.33(9)	3.79	9.45	2.17	1.115
8.43(13)	5.2680(9)	5.424(3)	19.21(11)	4.50	10.37	1.56	1.220
9.88(14)	5.2457(6)	5.405(2)	19.27(7)	3.26	8.49	2.19	1.220
11.71(18)	5.2344(6)	5.402(2)	19.17(7)	2.75	7.53	1.80	1.268
14.5(2)	5.1900(5)	5.3724(18)	19.12(7)	2.43	6.30	1.11	1.192

TABLE S2. Compressibility parameters calculated using PASCAL for experimental and DFT calculated results.

	Axes	K (TPa ⁻¹)	σK (TPa ⁻¹)	Empirical parameters			
				ϵ	λ	P_c	ν
Exp	a	2.6997	0.1342	0.0008	-0.0037	0.4024	0.8482
	b	2.1150	0.1046	0.0006	-0.0038	-0.4897	0.7306
	c	1.6427	0.2274	0.0	-0.0037	0.5765	0.6314
	V	6.0733	0.1915				
DFT	a	2.7334	0.0045	0.1231	0	-497.648	9.6142
	b	1.0187	0.0494	17.2944	-17.2633	-7.3077	0.0009
	c	1.2621	0.0403	8.567	-8.476	-17.4137	0.0037
	V	4.9735	0.1321				

TABLE S3. Second-order Birch-Murnaghan coefficients calculated using PASCAL.

	B_0 (GPa)	σB_0 (GPa)	V_0 (Å ³)	σV_0 (Å ³)	B'	$\sigma B'$	P_c (GPa)
Exp	135.3161	4.8459	581.0391	0.0934	4	N/A	0
DFT	165.2915	0.4932	573.0904	0.0787	4	N/A	0

S1. COMPUTATIONAL DETAILS

We performed first-principles simulations based on density functional theory (DFT) implemented within the VASP code [50, 51], version 6.3.2. PBEsol variant of generalised gradient approximation (GGA) [52] was employed as the exchange-correlation functional to accurately describe the structural properties of bulk $\text{Ca}_3\text{Ru}_3\text{O}_7$. We used PAW pseudopotentials (PBE, version 5.4) [53, 54] with 10 valence electrons for Ca ($3s^23p^24s^2$), 14 for Ru ($4p^64d^75s^1$), and 6 for O ($2s^22p^4$). An effective on-site Hubbard parameter $U_{\text{eff}} = 1.2$ eV was utilised to account for the correlation effects of the 4d electrons in Ru [55], reproducing the ambient-pressure structural and magnetic properties, as well as the band dispersion, in close agreement with previous experimental observations. Spin-orbit coupling (SOC) was included self-consistently within VASP. A plane wave cutoff of 800 eV and k -mesh grid of $8 \times 7 \times 2$ were used to resolve the total energies, forces, and stresses within 1 meV/f.u., 1 meV/Å, and 0.1 GPa, respectively. An energy convergence criterion of 10^{-9} eV was used for all the calculations and full structural relaxations were carried out till the Hellmann–Feynman forces on each atom were less than 1 meV/Å. Symmetry mode analyses were performed using the web-based ISOTROPY software suite [47]. Crystal structures as well as magnetic configurations were visualised with VESTA [56].

S2. DETERMINATION OF MAGNETIC GROUND STATE FROM DFT

To investigate the ground state magnetic configuration, we consider a ferromagnetic (FM) and 7 different antiferromagnetic (AFM) collinear spin arrangements shown in Fig. S1. Our collinear calculations without SOC reveal that F*-AFM corresponds to the ground state magnetic structure in agreement with previous theoretical and experimental findings [23, 25–27, 57, 59]. The obtained magnetic moment of 1.41 μ_B per Ru atom indicates the low-spin state of Ru^{4+} ions [57, 59]. Furthermore, our 0 K non-collinear calculations with SOC confirm the crystallographic b -axis as the easy direction for magnetization [23, 25–27, 57, 59].

TABLE S4. Relative energies (meV/f.u.) of the different collinear spin configurations considered in our DFT+ U calculations. $U_{\text{eff}} = 1.2$ eV is used for the Ru-5d orbitals without SOC.

A-AFM	A*-AFM	C-AFM	C*-AFM	G-AFM	G*-AFM	FM	F*-AFM
98.46	99.53	196.75	198.51	190.12	191.64	1.13	0.00

TABLE S5. Relative energies (meV/f.u.) of the F*-AFM magnetic configuration with different spin axes including SOC.

along a	along b	along c
2.38	0.00	6.62

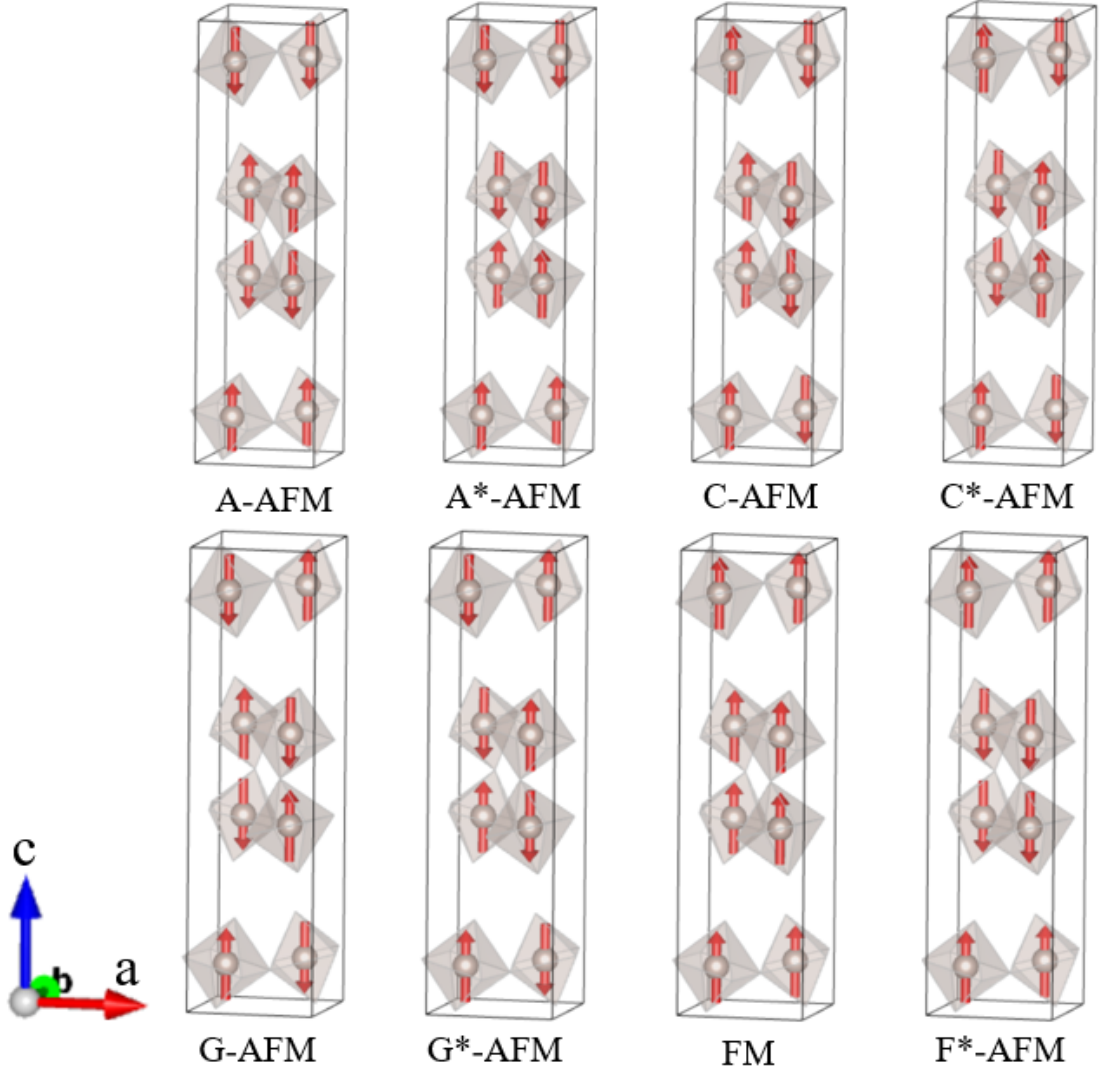


FIG. S1. Collinear spin configurations considered for determining the ground state magnetic structure of $\text{Ca}_2\text{Ru}_2\text{O}_7$. The grey spheres represent the Ru atoms and the red arrows indicate the spin magnetic moments on the Ru^{4+} ions.

S3. BAND STRUCTURE AT AMBIENT PRESSURE

Fig. S2 shows the electronic band structures computed for the $Bb2_1m$ structure of $\text{Ca}_3\text{Ru}_2\text{O}_7$ at ambient pressure with $U_{\text{eff}} = 1.2$ eV. We observe an overall metallic band structure with and without SOC. However, inclusion of SOC additionally opens up a local gap around the Γ -point observed in previous angle-resolved photoemission spectroscopy (ARPES) measurements [27, 58] highlighting the importance of SOC interaction in accurately describing the band structure at ambient pressure.

Our band structure results contradict previous PBEsol+ U studies that reported a band crossing around Γ with $U_{\text{eff}} = 1.2$ eV [57, 59]. To verify our findings, we have performed a full structural relaxation of the $Bb2_1m$ structure with SOC, which yielded an identical band structure featuring a partial gap at the Fermi level around the Γ -point. Thus, our results demonstrate that PBEsol functional with $U_{\text{eff}} = 1.2$ eV reliably reproduces the ambient-pressure band dispersion of $\text{Ca}_3\text{Ru}_2\text{O}_7$ closer to the experimental observations.

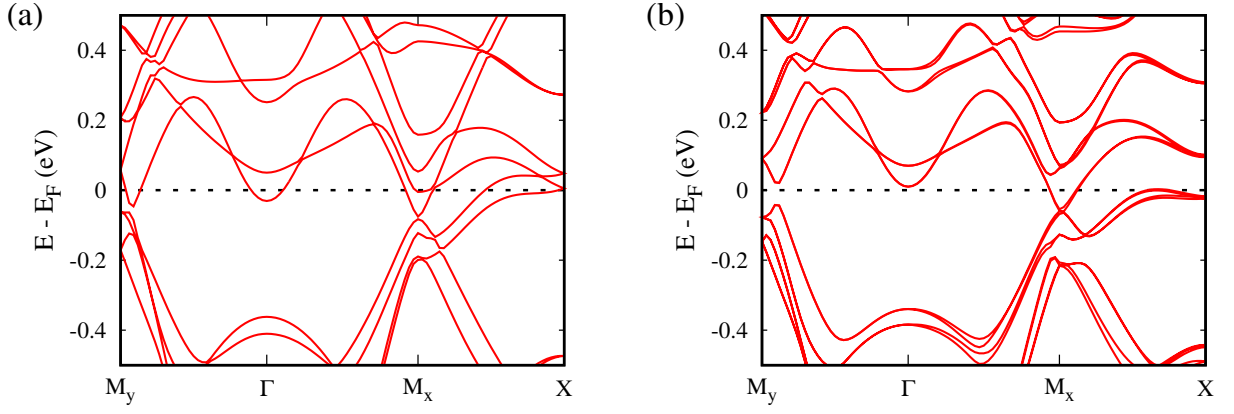


FIG. S2. Electronic band structure of $\text{Ca}_3\text{Ru}_2\text{O}_7$ at ambient pressure along the $M_y(0, 0.5, 0) - \Gamma(0, 0, 0) - M_x(0.5, 0, 0) - X(0.5, 0.5, 0)$ path calculated (a) without and (b) with SOC using a U_{eff} value of 1.2 eV.

S4. EVOLUTION OF THE PROPER VS. IMPROPER COMPONENT OF THE POLAR MODE WITH PRESSURE

As discussed in the main text, at low pressure, amplitude of the polar mode transforming as the Γ_5^- irrep in the DFT-calculated structures is in excess of that expected by the trilinear mechanism, suggesting that there is a small proper contribution to the polarisation at low pressure. To confirm this small additional proper component to the polarisation, we compute the polar mode amplitude for an $Fm2m$ structure containing only the Γ_5^- mode as a function of pressure. We show in Fig. S3 that the proper component vanishes when the hydrostatic pressure increases above 10 GPa.

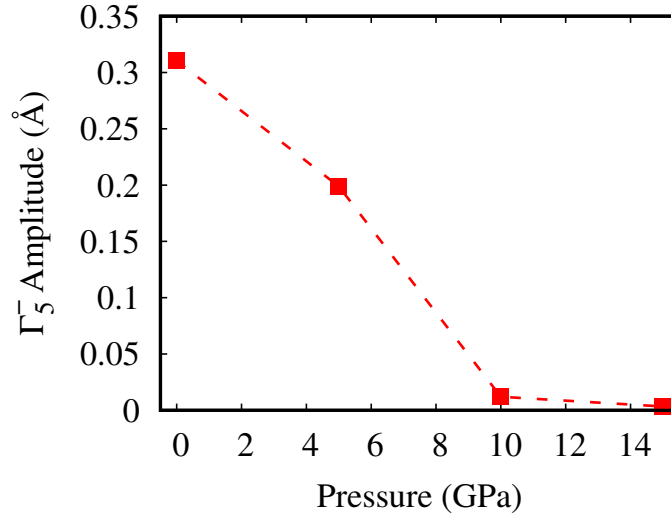


FIG. S3. Variation of the polar mode amplitude with pressure in the $Fm2m$ phase.

S5. EVOLUTION OF BAND STRUCTURE WITH PRESSURE

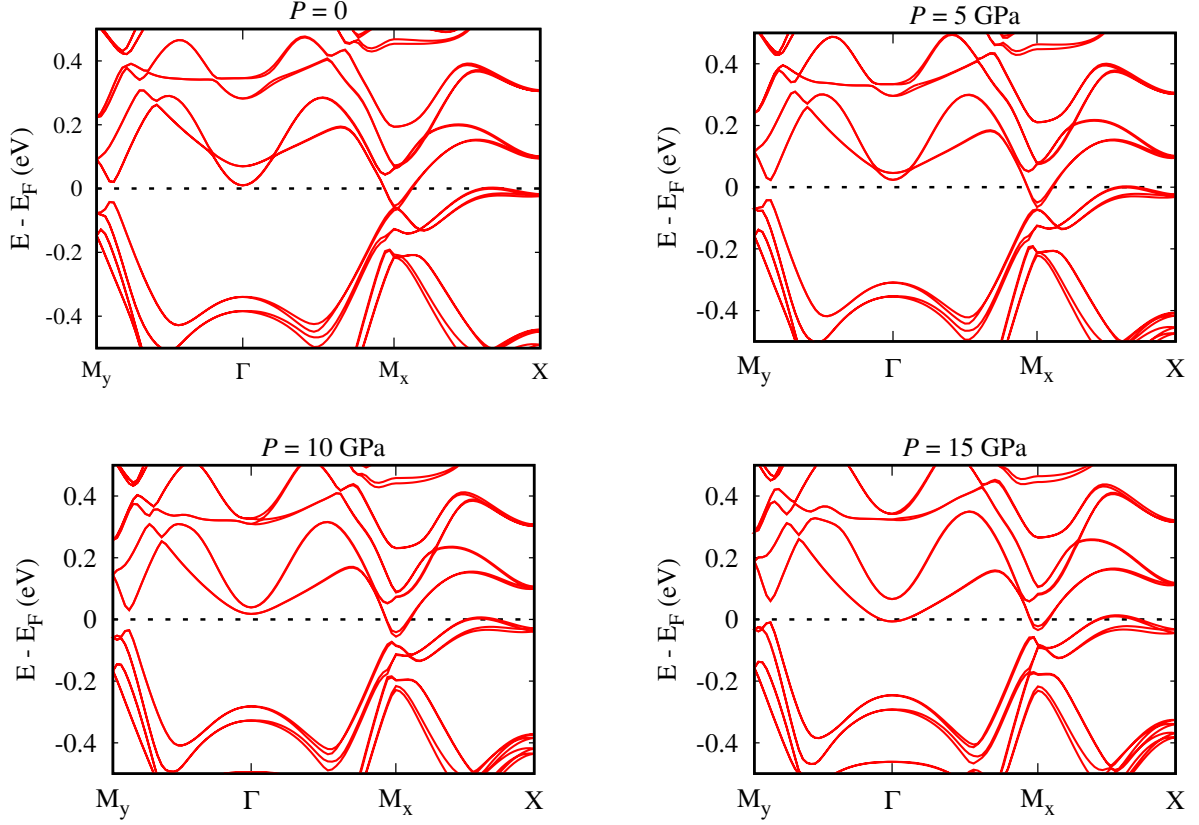


FIG. S4. Electronic band structure of $\text{Ca}_3\text{Ru}_2\text{O}_7$ as a function of pressure. SOC is included in all the calculations.

S6. EVOLUTION OF THE MAGNETIC MOMENT WITH PRESSURE

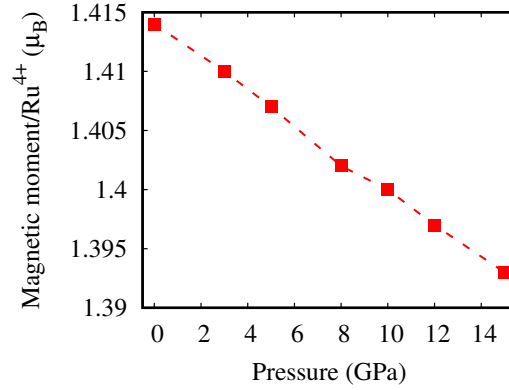


FIG. S5. Spin magnetic moment on the Ru^{4+} ions as a function of pressure obtained from collinear calculations without SOC.

Our non-collinear calculations including SOC confirm that the b -axis remains the easy magnetisation direction throughout the 0 – 15 GPa pressure range considered in our work.

S7. CHANGE IN THE RASHBA SPIN-SPLITTING WITH PRESSURE

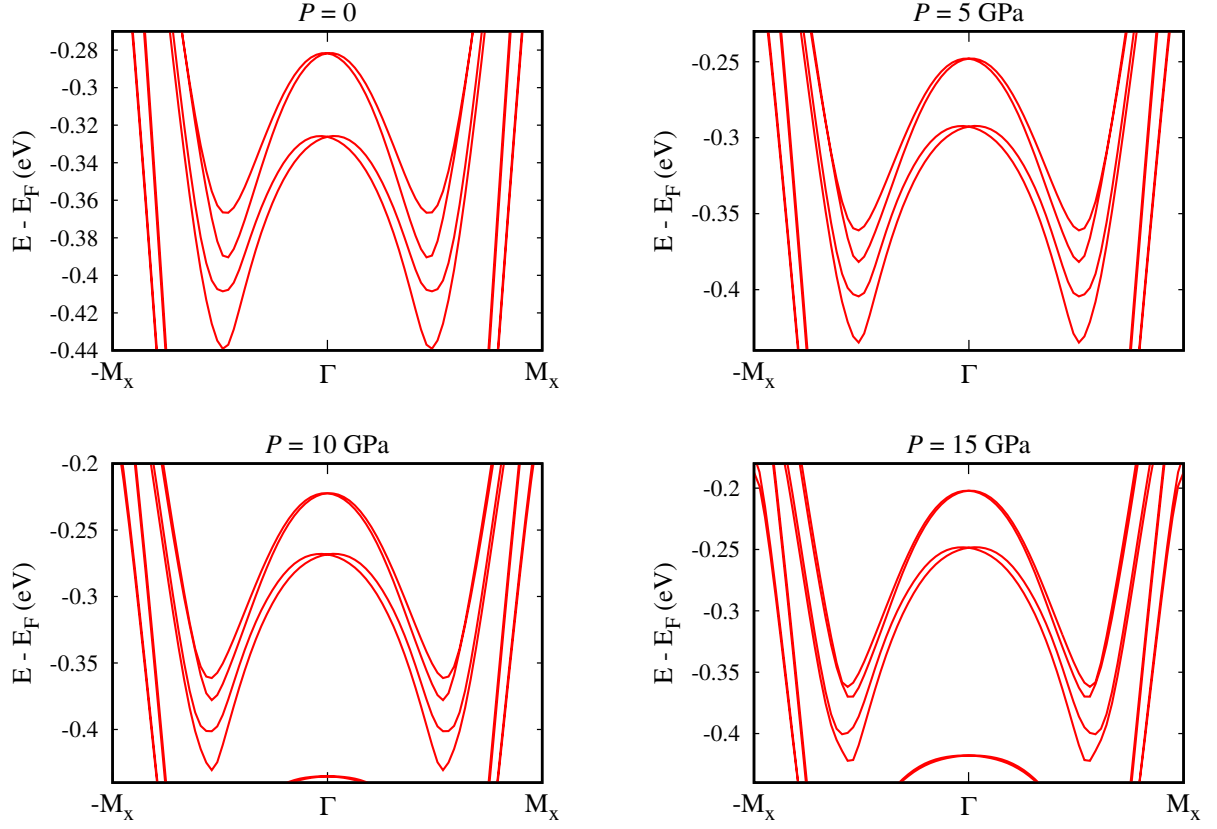


FIG. S6. Electronic band structures at different hydrostatic pressure, showing the decrease in the Rashba spin-splitting at the VBM as a function of pressure.

To understand the decrease in the Rashba splitting with pressure, depicted in Fig. S6, we compute the ambient-pressure band structure by setting the polar mode amplitude to zero, as shown in Fig. S7. Note that even in the absence of the polar mode, the two tilt modes collectively polarise the electron clouds, leading to inversion symmetry breaking and thus preserving the $Bb2_1m$ structure. We find that the absence of the polar mode leads to a substantial enhancement of the Rashba parameter to ~ 172 meV \AA , which is approximately 1.8 times greater than its value in the relaxed $Bb2_1m$ structure containing the polar mode as well as the two tilt modes (at zero pressure). This suggests that the increasing polar mode amplitude as a function of pressure (discussed in the main text) is responsible for the reduction in the Rashba spin-splitting observed in Fig. S6. Additionally, the spin-projected band structures in Fig. S7(b-d) reveal the splitting between spin-up and spin-down bands for the x - and y - spin-components, confirming the pure Rashba character of the bands at the VBM [49].

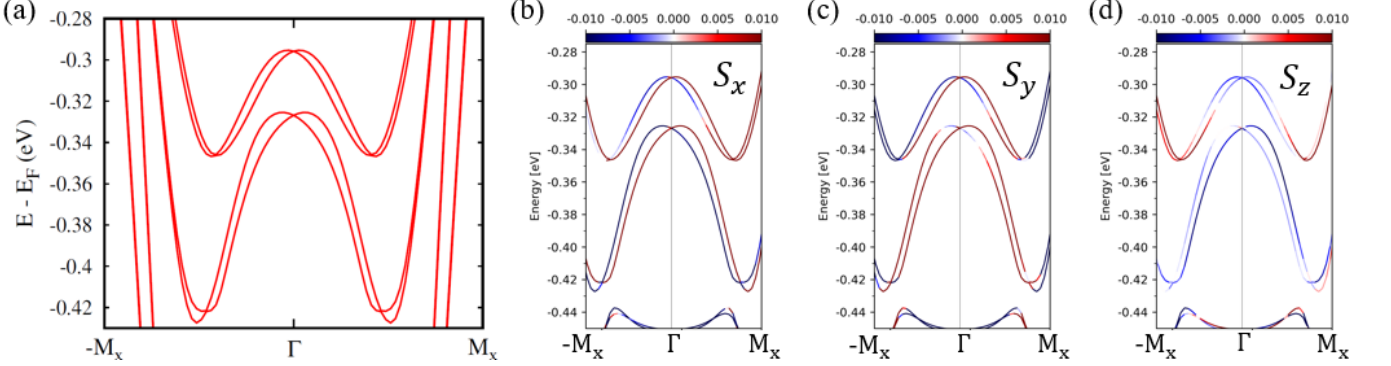


FIG. S7. (a) Band structure at ambient pressure calculated by setting the polar mode amplitude to zero (tilts only). (b-d) Corresponding spin-resolved band structures confirming the pure Rashba character of the bands at the VBM.